

Article

# Dynamic Response Characterization of Floating Structures Based on Numerical Simulations

Francisco Pimenta <sup>1</sup>, Carlo Ruzzo <sup>2</sup>, Giuseppe Failla <sup>3</sup>, Felice Arena <sup>2</sup>, Marco Alves <sup>4</sup>  
and Filipe Magalhães <sup>1\*</sup>

<sup>1</sup> CONSTRUCT-ViBest, Faculty of Engineering, University of Porto, 4200-465 Porto, Portugal; ec09176@fe.up.pt

<sup>2</sup> Natural Ocean Engineering Laboratory (NOEL), Mediterranean University of Reggio Calabria, 89122 Reggio Calabria, Italy; carlo.ruzzo@unirc.it (C.R.); arena@unirc.it (F.A.)

<sup>3</sup> DICEAM Department, Mediterranean University of Reggio Calabria, 89122 Reggio Calabria, Italy; giuseppe.failla@unirc.it

<sup>4</sup> WavEC Offshore Renewables, 1350-352 Lisbon, Portugal; marco@wavec.org

\* Correspondence: filipema@fe.up.pt

Received: 24 August 2020; Accepted: 22 October 2020; Published: 29 October 2020



**Abstract:** Output-only methods are widely used to characterize the dynamic behavior of very diverse structures. However, their application to floating structures may be limited due to their strong nonlinear behavior. Therefore, since there is very little experience on the application of these experimental tools to these very peculiar structures, it is very important to develop studies, either based on numerical simulations or on real experimental data, to better understand their potential and limitations. In an initial phase, the use of numerical simulations permits a better control of all the involved variables. In this work, the Covariance-driven Stochastic Subspace Identification (SSI-COV) algorithm is applied to numerically simulated data of two different solutions to Floating Offshore Wind Turbines (FOWT) and for its capability of tracking the rigid body motion modal properties and susceptibility to different modeling restrictions and environmental conditions tested. The feasibility of applying the methods in an automated fashion in the processing of a large number of datasets is also evaluated. While the structure natural frequencies were consistently obtained from all the simulations, some difficulties were observed in the estimation of the mode shape components in the most changing scenarios. The estimated modal damping coefficients were in good agreement with the expected results. From all the results, it can be concluded that output-only methods are capable of characterizing the dynamic behavior of a floating structure, even in the context of continuous dynamic monitoring using automated tracking of the modal properties, and should now be tested under uncontrolled environmental loads.

**Keywords:** operational modal analysis; output-only identification methods; SSI-COV; automated operational modal analysis; floating structures; spar buoy; semi-submersible

## 1. Introduction

Among engineering structures, floating platforms are a very important category. Historically, moored floating structures have been widely used in coastal areas (e.g., for harbor jetties, floating breakwaters, etc.) and open-sea (mainly for oil and gas platforms at water depths >500 m). Currently, many vectors, including the needs for renewable energy production, space occupation, and the reduction of the visual/environmental impact of human activities, are pushing towards the radical innovation and growth of floating structures. In this context, Floating Offshore Wind Turbines (FOWTs) are some of the most mature technologies. In the last decade, a huge effort has

been made in the development and industrialization of FOWT concepts [1–4], leading to the recent realization of the first floating wind farms, such as Statoil’s “Hywind Scotland” farm [5] and Windfloat Atlantic on the Portuguese coast [6]. Other innovative concepts, including, e.g., Multi-Purpose floating Platforms (MPPs) [7,8] and Very Large Floating Structures (VLFs) [9,10], are being intensively investigated as well. This would allow moving offshore not only renewable energy production (wind, wave, current, etc.), but also other activities, including aquaculture [11,12], desalinization [13], hydrogen production [14], etc., with potentially significant advantages from the economic, social, and environmental points of view. Although different floating concepts have reached different stages of development, namely the Technology Readiness Level (TRL), experimental investigations are of foremost importance to better understand their complex dynamic behavior, validate numerical models, demonstrate the technical/industrial feasibility of new concepts, and optimize the design in order to improve cost-effectiveness (i.e., reduce the levelized cost of energy (LCOE) which is currently the main drawback of this emergent industry). Traditionally, experimental activities with floating concepts are carried out in wave tanks and ocean basins [15–17], where scaled models are subject to controlled input load conditions. However, the demand for larger scale factors (TRL 5-7) and the high costs of indoor activities could be addressed through intermediate-scale experiments at sea [18]. Although similar to prototypical tests, these activities would need specific identification techniques to achieve a detail comparable to indoor experiments in spite of the uncontrolled environment. References [19,20] carried out a 1:30 at-sea experiment of the UMaine-Hywind spar FOWT concept [21] and successfully identified the heave/roll/pitch hydrodynamic properties of the structure over a wide range of different environmental conditions. By doing so, they proved the feasibility of at-sea experiments on floating structures, but they also highlighted the need for developing opportune output-only identification techniques to support the interpretation of the experimental data in an uncontrolled environment.

The methods for output-only (or operational) modal analysis are already quite mature. Currently, a considerable range of methods is available, and some of them can be combined with routines that permit their automation and, so, their use in the context of continuous monitoring [22]. Their application in the context of floating structures is very limited and at the same time very challenging, since not all the theoretical assumptions of the methods are fulfilled. It is very important to understand, if in spite of the partial violation of some assumptions, reasonable results can still be obtained [22]. Based on some numerical studies on a spar wind turbine, Ruzzo et al. [23,24] showed that the Frequency-Domain Decomposition (FDD) output-only method may be feasible for the dynamic identification of the rigid body motions of the platform under hydrodynamic loads. However, the method requires the natural frequency of the structure to be far from those of the exciting loads and the output record duration to be sufficiently long, and it is not a method that is suitable for automated tracking of modal properties. In this paper, a more sophisticated parametric algorithm, the SSI-COV output-only identification technique, is applied to datasets provided by numerical simulations of two different FOWT concepts, namely the OC4-DeepCwind semi-submersible platform [25] and UMaine-Hywind spar [5]. The effects of several parameters on the capability of the method to identify the dynamic properties of the two systems, attaining the rigid body motions under various input loads, have been investigated. Such parameters include coupling between different Degrees Of Freedom (DOFs), wave direction and significant height, structural symmetry, structure nonlinearity, wave spectrum narrow-bandedness, and output time history duration. The results obtained are very encouraging and provide practical indications in view of the output-only identification of real structure models in uncontrolled environments. The proposed identification method is very promising also for other applications relative to full-scale structures, such as structural health monitoring, with continuous tracking of the modal properties.

Firstly, a brief description of the SSI-COV method will be given, followed by a description of the numerical models used. The method will be tested in a limited number of simulations to make a preliminary evaluation of the influence of modeling choices and wave scenarios on the obtained

results. After that, the method will be extended to a large number of simulations, where an automated analysis must be used. Finally, the principal conclusions will be highlighted.

## 2. Method for Operational Modal Analysis

One important goal of this work is to show that the modal parameters of floating structures can be identified in an automated way using the measured response of the structure only, since this is crucial in the context of continuous monitoring programs for the identification of structural changes. Although methods based on spectral analysis are capable of identifying the natural frequencies [23,24], they are not suitable for the automatic identification of the natural frequencies. To overcome this limitation, the SSI-COV method will be used to characterize the dynamic behavior of the structure.

The SSI-COV method depends on some user-defined parameters to provide the best results. While this task can easily be manually performed for a limited number of datasets, it is not feasible for very large amounts of data, where automated procedures must be used. For the remainder of this section, the SSI-COV method's principal aspects will be briefly described, as well as how it can be applied within an automated analysis procedure.

### 2.1. SSI-COV

The SSI-COV method (Covariance-driven-Stochastic Subspace Identification) is one of the most reliable methods for output-only modal identification. Since this method was fully described in [26], here, only the most relevant steps are presented. It is a parametric method in the time domain that fits a state space model [27] to the recorded response ( $\mathbf{y}_k$ ):

$$\begin{cases} \mathbf{x}_{k+1} = \mathbf{A} \cdot \mathbf{x}_k + \mathbf{w}_k \\ \mathbf{y}_k = \mathbf{C} \cdot \mathbf{x}_k + \mathbf{v}_k \end{cases} \quad (1)$$

where  $\mathbf{x}_k$  is the state vector and  $\mathbf{w}_k$  and  $\mathbf{v}_k$  the process and measurement noise, respectively.

Having defined the state-space model, the state matrix  $\mathbf{A}$  contains all the relevant dynamic information of the system and can be computed from the correlation matrix calculated from the response of the instrumented DOFs, defined as:

$$\mathbf{R}_y(j) = E[\mathbf{y}_{k+j} \cdot \mathbf{y}_k^T] = \mathbf{C} \cdot \mathbf{A}^{j-1} \cdot \mathbf{G} = \mathbf{C} \cdot \mathbf{A}^{j-1} \cdot E[\mathbf{x}_{k+1} \cdot \mathbf{y}_k^T] \quad (2)$$

The correlation matrices can be distributed in a Toeplitz matrix such that:

$$\mathbf{T}_{(1|j_i)} = \begin{bmatrix} \mathbf{R}_{j_i}^{ref} & \mathbf{R}_{j_i-1}^{ref} & \cdots & \mathbf{R}_1^{ref} \\ \mathbf{R}_{j_i+1}^{ref} & \mathbf{R}_{j_i}^{ref} & \cdots & \mathbf{R}_2^{ref} \\ \vdots & \vdots & \ddots & \vdots \\ \mathbf{R}_{2 \cdot j_i-1}^{ref} & \mathbf{R}_{2 \cdot j_i-2}^{ref} & \cdots & \mathbf{R}_{j_i}^{ref} \end{bmatrix} = \begin{bmatrix} \mathbf{C} \\ \mathbf{C} \cdot \mathbf{A} \\ \vdots \\ \mathbf{C} \cdot \mathbf{A}^{j_i-1} \end{bmatrix} \cdot \begin{bmatrix} \mathbf{A}^{j_i-1} \cdot \mathbf{G} & \cdots & \mathbf{A} \cdot \mathbf{G} & \mathbf{G} \end{bmatrix} \quad (3)$$

The Toeplitz matrix from Equation (3) can be decomposed according to:

$$\mathbf{T}_{(1|j_i)} = \begin{bmatrix} \mathbf{U}_1 & \mathbf{U}_2 \end{bmatrix} \cdot \begin{bmatrix} \mathbf{S}_1 & \mathbf{0} \\ \mathbf{0} & \mathbf{0} \end{bmatrix} \cdot \begin{bmatrix} \mathbf{V}_1^T \\ \mathbf{V}_2^T \end{bmatrix} \quad (4)$$

where the only non-zero values of the singular value decomposition are marked with the index 1. As the Toeplitz matrix can be written from the observability ( $\mathbf{O}$ ) and controllability ( $\mathbf{\Gamma}$ ) matrices, these can be defined to be:

$$\begin{cases} \mathbf{O}_{j_i} = \mathbf{U}_1 \cdot \mathbf{S}_1^{\frac{1}{2}} \\ \mathbf{\Gamma}_{j_i} = \mathbf{S}_1^{\frac{1}{2}} \cdot \mathbf{V}_1^T \end{cases} \longrightarrow \mathbf{T}_{(1|j_i)} = \mathbf{O}_{j_i} \cdot \mathbf{\Gamma}_{j_i} \quad (5)$$

Comparing Equations (3) and (5), it can be easily shown that the output matrix  $\mathbf{C}$  can be computed from the first  $n$  lines of the observability matrix,  $n$  being the number of DOFs of the system. Having the output matrix defined, the corresponding state matrix results from an optimization problem since:

$$\begin{bmatrix} \mathbf{C} \\ \mathbf{C} \cdot \mathbf{A} \\ \vdots \\ \mathbf{C} \cdot \mathbf{A}^{j_i-2} \end{bmatrix} \cdot \mathbf{A} = \begin{bmatrix} \mathbf{C} \cdot \mathbf{A} \\ \mathbf{C} \cdot \mathbf{A}^2 \\ \vdots \\ \mathbf{C} \cdot \mathbf{A}^{j_i-1} \end{bmatrix} \longrightarrow \mathbf{A} = \begin{bmatrix} \mathbf{C} \\ \mathbf{C} \cdot \mathbf{A} \\ \vdots \\ \mathbf{C} \cdot \mathbf{A}^{j_i-2} \end{bmatrix}^{\dagger} \cdot \begin{bmatrix} \mathbf{C} \cdot \mathbf{A} \\ \mathbf{C} \cdot \mathbf{A}^2 \\ \vdots \\ \mathbf{C} \cdot \mathbf{A}^{j_i-1} \end{bmatrix} \quad (6)$$

Having the state matrix identified, the mode shape components, natural frequencies, and modal damping ratios follow directly from its eigendecomposition [26]:

$$\mathbf{A} = \mathbf{\Psi} \cdot \mathbf{\Lambda}_D \cdot \mathbf{\Psi}^{-1} \quad (7)$$

where  $\mathbf{\Psi}$  contains the mode shape components in its columns and  $\mathbf{\Lambda}_D$  is diagonal with the discrete time eigenvalues ( $\mu_k$ ), related to the natural frequencies ( $\omega_k$ ) and modal damping coefficients ( $\xi_k$ ) by [26]:

$$\begin{cases} \lambda_k = \frac{\ln \mu_k}{\Delta t} \\ \lambda_k, \lambda_k^* = -\xi_k \cdot \omega_k \pm i \cdot \sqrt{1 - \xi_k^2} \cdot \omega_k \end{cases} \longrightarrow \begin{cases} \omega_k = |\lambda_k| \\ \xi_k = -\frac{\Re(\lambda_k)}{|\lambda_k|} \end{cases} \quad (8)$$

When real observation data are used, the number of non-zero singular values of the Toeplitz matrix, or model order, is not clearly defined as a significant number of poles may be needed to properly model the noise and the load frequency content induced in the response. As this value is a priori unknown, a common procedure in operational modal analysis is to test different model orders, keeping only the modes that are consistently obtained, regardless of the order used. If the poles (frequencies) obtained are plotted as a function of the model order, a stabilization diagram is created (see Figure 3 in Section 4.1), where the stable poles should become clear. If the number of datasets to be analyzed is limited, the final estimates of the modal properties can be manually selected from the stabilization diagrams; if not, as happens in the context of continuous dynamic monitoring, the analysis of the stabilization diagrams should be automated as described in the following section.

## 2.2. Automated Operational Modal Analysis

Having presented the main characteristics of the method that will be used, it is important to provide a brief description of how it can be applied to large volumes of data. As described in [28], it is possible to use a cluster analysis, grouping the similar modes together. The Euclidean distance between two modes obtained in two different model orders can be computed as:

$$d_{i-j} = \alpha \cdot \left| \frac{f_i - f_j}{f_j} \right| + \beta \cdot (1 - MAC_{i,j}) \quad (9)$$

where  $f_i$  and  $f_j$  are the mode frequencies,  $MAC_{i,j}$  is the modal assurance criterion [29] between the mode shapes, which evaluates the similarity of the mode shapes, and  $\alpha$  and  $\beta$  are weighting coefficients to be tuned in each application. The defined criteria allow the construction of a hierarchical tree that must be provided with some stoppage criteria with respect to the differences inside a given cluster. Evidently, the more restricted the criteria, the higher the number of clusters obtained, which can make the distinction between real and spurious modes more difficult. Finally, having the clusters defined,

the tracking of a specific mode shape can be made comparing the different cluster mean value with a reference frequency and mode shape. These reference values should be tuned in each application from either theoretical values or a good quality experimental setup.

### 3. Numerical Models

#### 3.1. NREL 5 MW Semi-Submersible Floating Offshore Wind Turbine

The NREL 5 MW semi-submersible floating offshore wind turbine was modeled using the FAST certification test files [25,30]. The structure is constituted by a central cylinder and 3 eccentric cylinders placed at the vertexes of a 50 m side equilateral triangle. While the first one connects to the tower 10 m over the Still Water Level (SWL), the remaining elevate themselves 12 m above the SWL. All the cylinders are connected by a tubular structure, and the structure's total draft is 20 m. From the detailed geometric and mechanical properties available in [25,30], it was possible to build the equivalent structural model in ANSYS® AQWA, with the overall properties summarized in Table 1, represented in Figure 1. In this regard, it should be noted that all the DOFs of the model refer to the Center of Gravity (CoG).

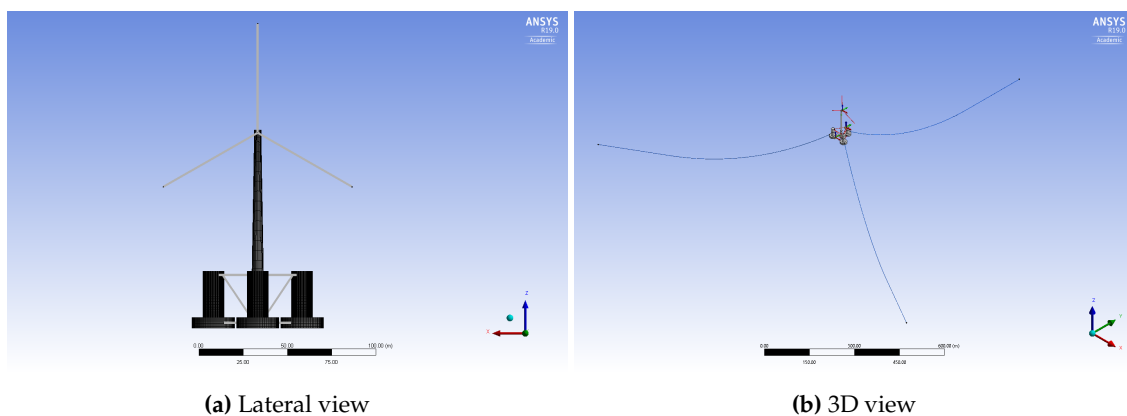


Figure 1. ANSYS® AQWA model lateral view and 3D representation.

Table 1. Main characteristics of the 5 MW NREL structural model implemented in AQWA.

Parameter	Value	Units
Overall mass	$1.389 \times 10^7$	kg
CoG position $x_G$	0	m
CoG position $y_G$	0	m
CoG position $z_G$	-9.85	m
Mass moment of inertia $I_{xx}$	$1.132 \times 10^{10}$	kg·m <sup>2</sup>
Mass moment of inertia $I_{yy}$	$1.131 \times 10^{10}$	kg·m <sup>2</sup>
Mass moment of inertia $I_{zz}$	$1.229 \times 10^{10}$	kg·m <sup>2</sup>

Here, the cylinders and the turbine tower are dealt with as pure diffracting bodies, i.e., by means of potential theory and neglecting viscous forces. To include the viscous drag contribution absent from the model, a quadratic drag damping matrix  $\mathbf{C}_{quad}$  was added to the model, defined in coherent units [31]:

$$\mathbf{C}_{quad} = \begin{bmatrix} 3.95 \times 10^5 & 0 & 0 & 0 & 0 & 0 \\ 0 & 3.95 \times 10^5 & 0 & 0 & 0 & 0 \\ 0 & 0 & 3.88 \times 10^6 & 0 & 0 & 0 \\ 0 & 0 & 0 & 3.70 \times 10^{10} & 0 & 0 \\ 0 & 0 & 0 & 0 & 3.70 \times 10^{10} & 0 \\ 0 & 0 & 0 & 0 & 0 & 4.08 \times 10^9 \end{bmatrix} \quad (10)$$

Differently, the tubular bracings are modeled as pure Morison elements, with added mass and drag coefficients  $C_a = 1$  and  $C_d = 1$ , respectively. Hydrodynamic forces on Morison elements are computed by the software according to:

$$\mathbf{f}(t) = (1 + C_a) \cdot \rho \cdot \pi \cdot R^2 \cdot \mathbf{a}(t) - C_a \cdot \rho \cdot \pi \cdot R^2 \cdot \dot{\mathbf{u}}(t) + C_d \cdot \rho \cdot R \cdot |\mathbf{v}(t) - \dot{\mathbf{u}}(t)|(\mathbf{v}(t) - \dot{\mathbf{u}}(t)) \quad (11)$$

$\mathbf{f}$  being the hydrodynamic unit force vector on a bracing segment;  $\rho = 1025 \text{ kg} \cdot \text{m}^{-3}$  the seawater density;  $R$  the bracing radius;  $\mathbf{v}$  and  $\mathbf{a}$  the time-dependent wave velocity and acceleration vectors normal to the structure; and  $\mathbf{u}$  the structure motion vector, which appears by means of its time derivatives, i.e., structure velocity and acceleration. Total hydrodynamic forces, where no second order forces have been considered, are obtained by integrating Equation (11) over all the bracings.

The mooring system is represented by three nonlinear catenary lines, whose main characteristics are summarized in Table 2. Again, Equation (11) is used for the calculation of hydrodynamic forces on the mooring lines.

**Table 2.** Main characteristics of the 5 MW NREL mooring system implemented in AQWA.

Parameter	Value	Units
Water depth	200	m
Horizontal distance anchor-fairlead	796.7	m
Vertical distance anchor-fairlead	186.0	m
Linear line weight	113.35	$\text{kg} \cdot \text{m}^{-1}$
Line length	835.35	m
Equivalent line diameter	0.0766	m
Transverse drag coefficient of the line	2	-
Longitudinal drag coefficient of the line	0.4	-
Added mass coefficient of the line	0.8	-
Line stiffness	$7.536 \times 10^8$	N

The overall equation of motion of the structure in the time domain is:

$$(\mathbf{M} + \mathbf{A}_\infty)\ddot{\mathbf{u}}(t) + \int_0^t \left\{ \int_0^\infty \mathbf{B}(\omega) \cos[\omega(t - \tau)] d\omega \right\} \dot{\mathbf{u}}(\tau) d\tau + \mathbf{K}(\mathbf{u})\mathbf{u}(t) = \mathbf{f}_{nl}(t, \mathbf{u}, \dot{\mathbf{u}}, \ddot{\mathbf{u}}) \quad (12)$$

$\mathbf{M}$  being the structural mass matrix,  $\mathbf{A}_\infty$  the added mass matrix for infinite frequency,  $\mathbf{B}$  the frequency-dependent radiation damping, and  $\mathbf{K}$  the hydrostatic restoring coefficients' matrix, and all the nonlinear effects, as viscous damping, mooring forces, externally applied loads or second order wave forces, have been included in  $\mathbf{f}_{nl}$ . Aerodynamic forces on the rotor-nacelle assembly and on the tower were completely neglected. Equation (12) has 6 DOF, corresponding to the rigid body motions of the floating structure, namely surge, sway, heave, roll, pitch, and yaw. However, reduced/simplified forms of the same equation can be obtained by considering only a subset of DOF, if deemed opportune. It should be noted that mooring lines and bracings contribute to the overall equation of motion with nonlinear terms, namely horizontal restoring forces and viscous drag forces. It follows that the numerical model is overall nonlinear, which is a very important feature for the investigation of automated OMA efficiency in realistic application cases.

### 3.2. UMaine-Hywind 5 MW Spar Floating Offshore Wind Turbine

The second case study refers to the UMaine-Hywind 5 MW spar floating offshore wind turbine. This concept is based on another FAST test case [32], namely the OC3-Hywind spar, which is widely regarded as a reference design for a 5 MW spar floating offshore wind turbine. The UMaine-Hywind has the exact same support structure of OC3-Hywind, but a smaller mooring system, aimed to work at a water depth of 200 m instead of 320 m, as detailed in [21]. The structure is a ballast-stabilized vertical tapered cylinder, with a total draft of 120 m. The main characteristics of the structure are reported in

Table 3 and the numerical model represented in Figure 2. Furthermore, in this case, all the DOFs of the model refer to the CoG.

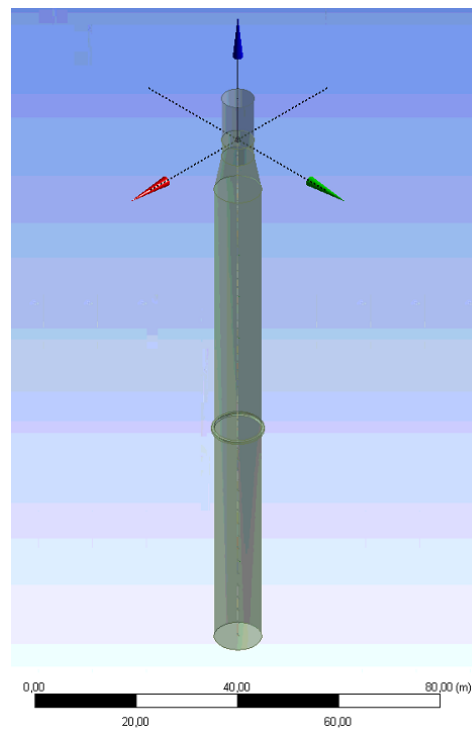


Figure 2. OC3-Hywind spar floating offshore wind turbine numerical model.

Table 3. Main characteristics of the UMaine-Hywind structural model implemented in AQWA.

Parameter	Value	Units
Diameter $D_{min}, D_{max}$	6.5; 9.4	m
Taper position $z_{min}, z_{max}$	-4; -12	m
Overall mass	$8.066 \times 10^6$	kg
Center of gravity (CoG) position $x_G = y_G$	0	m
Center of gravity (CoG) position $z_G$	-78	m
Mass moment of inertia $I_{xx}$	$2.189 \times 10^{10}$	kg·m <sup>2</sup>
Mass moment of inertia $I_{yy}$	$2.419 \times 10^{10}$	kg·m <sup>2</sup>
Mass moment of inertia $I_{zz}$	$1.181 \times 10^8$	kg·m <sup>2</sup>

As per the previous case study, the structure model was implemented in ANSYS® AQWA, and no second order forces were considered. The numerical model is consistent with the one used in [19], which was validated against experimental data collected at sea on a 1:30 physical model of a spar structure. With respect to the previous case, a linearized approach was used for hull modeling, which is represented by means of 104 Morison elements, with added mass and drag coefficients  $C_a = 0.97$  and  $C_d = 0$ , respectively. This is because the aim of the analysis of this structure is limited to the investigation of the effects of wave spectrum narrow-bandedness and record duration on OMA output-only identification procedures.

Although the viscous drag forces are negligible with respect to the inertial ones in absolute, justifying the  $C_d = 0$  assumption undertaken in the model, they are the main source of damping for the floating spar structure. Consequently, they were represented by means of a linearized damping matrix  $\mathbf{C}_{damp}$ , based on the approach proposed by Siow et al. [33]. The drag term of the Morison equation, i.e., the last term of Equation (11), can be indeed rewritten as:

$$\mathbf{f}_d(t) = C_d \cdot \rho \cdot R \cdot [|\mathbf{v}(t)| \cdot \mathbf{v}(t) - |\mathbf{v}(t)| \cdot \dot{\mathbf{u}}(t)] \quad (13)$$

by assuming that the structural velocity is much smaller than the wave particle velocity. It could be noted that the vector notation of Equation (13) can be simplified by considering the z-dependent horizontal forces and velocities, as the spar structure is not supposed to deviate much from the vertical layout. Further, it can be expanded in Fourier series, obtaining the following linear expression:

$$f_{d,h}(z,t) = C_d \cdot \rho \cdot R(z) \frac{8 \cdot v_{max}(z)}{3\pi} v_h(z,t) - C_d \cdot \rho \cdot R(z) \cdot \frac{8 \cdot v_{max}(z)}{3\pi} \cdot [\dot{u}_1(t) - (z - z_G)\dot{u}_5(t)] \quad (14)$$

where  $u_1$  and  $u_5$  are respectively the surge and pitch motions of the structure, arbitrarily intending the x-axis as parallel to the wave direction. The first term of Equation (14) is the linearized drag force, which is much smaller than the inertia terms of Equation (11) and is hence neglected in the model. The second term is instead the wave-dependent linearized drag damping and was used to build the linearized damping matrix  $C_{damp}$ , as follows:

$$C_{damp} = \int_{z_{min}}^0 C_d \cdot \rho \cdot R(z) \cdot \frac{8 \cdot v_{max}(z)}{3\pi} \cdot \begin{bmatrix} 1 & 0 & 0 & 0 & z - z_G & 0 \\ 0 & 1 & 0 & z - z_G & 0 & 0 \\ 0 & 0 & 0 & 0 & 0 & 0 \\ 0 & z - z_G & 0 & (z - z_G)^2 & 0 & 0 \\ z - z_G & 0 & 0 & 0 & (z - z_G)^2 & 0 \\ 0 & 0 & 0 & 0 & 0 & 0 \end{bmatrix} dz \quad (15)$$

Finally, the total wave-dependent linearized objective damping matrix  $C_{obj}$  was obtained by summing  $C_{damp}$  to the additional damping terms estimated experimentally by Jonkman [32] for the OC3-Hywind spar, i.e.,  $C_{11} = C_{22} = 1.0 \times 10^5 \text{ Nsm}^{-1}$ ;  $C_{33} = 1.3 \times 10^5 \text{ Nsm}^{-1}$ , and  $C_{66} = 1.3 \times 10^7 \text{ Nmsrad}^{-1}$ . In practice, the linearized damping matrix of the numerical model was assessed as follows:

1. the modal analysis of the system was carried out by considering the overall mass matrix and the linearized stiffness matrix (taking into account also the mooring system);
2. the objective damping matrix  $C_{obj}$  was obtained for a reference wave condition, i.e., an Airy wave with height  $H = 6 \text{ m}$  and period  $T = 10 \text{ s}$ ;
3. a set of modal damping ratios was assessed by tuning the theoretical damping matrix  $C$  of the ideal classically-damped linear system obtained against the objective matrix  $C_{obj}$ ;
4. the matrix  $C$  was used as an input in ANSYS<sup>®</sup> AQWA.

The resulting modal properties obtained for the linearized system in ANSYS<sup>®</sup> AQWA are reported in Table 4.

**Table 4.** Modal properties of the 6 rigid motion modes, including angular frequencies, natural frequencies, modal damping ratios, and 6 mode shape components of the spar numerical model implemented in ANSYS<sup>®</sup> AQWA (X-surge; Y-sway; Z-heave; RX-roll; RY-pitch; RZ-yaw).

Mode	$\omega$	$f$	$\zeta$	Mode Shapes Components					
	(mrad/s)	(mHz)	(%)	X	Y	Z	RX	RY	RZ
1	62.11	9.885	11	1	0	0	0	0	0
2	71.44	11.37	8	0	1	0	0	0	0
3	194.8	31.00	2	0.99	0	0	0	-0.13	0
4	201.6	32.09	3	0	0.99	0	-0.13	0	0
5	203.6	32.40	4	0	0	0	1	0	0
6	912.4	145.21	6	0	0	0	0	0	1

The mooring system is represented by three nonlinear catenary lines, whose main characteristics are summarized in Table 5. In this case, to preserve the linearized damping behavior of the overall model, the hydrodynamic coefficients of the lines were set to 0.

**Table 5.** Main characteristics of the UMaine-Hywind mooring system implemented in ANSYS® AQWA.

Parameter	Value	Units
Water depth	200	m
Distance anchor-fairlead	439.8	m
Linear line weight	145	kg·m <sup>-1</sup>
Line length	468	m
Line stiffness	$3.842 \times 10^8$	N

#### 4. Results

Having described the adopted numerical models, several numerical simulations were carried out and the dynamic properties estimated from the correspondent response time series.

##### 4.1. The 5 MW NREL Semi-Submersible Floating Offshore Wind Turbine

The NREL 5 MW floating platform model was used to test the limitations of this type of approach to a floating structure, with its strongly non-linear behavior. To do so, seven-thousand two-hundred seconds of wave excitation time series were generated (7500 minus 300 s to damp out any transient component of the response) with the following properties:

- T1-yaw, sway and roll DOF blocked; waves in the surge direction;
- T2-yaw DOF blocked; waves in the surge direction;
- T3-all DOF active; waves in the surge direction;
- T4-yaw DOF blocked; waves at 45°;
- T5-all DOF active; waves at 45°;
- T6-all DOF active; waves at 45°; Cable 1 stiffness reduced to 10% of its original value;

The stabilization and damping diagrams obtained with the SSI-COV method are presented in Figure 3 for Simulations T1, T2, and T3, and in Figure 4 for Simulations T4, T5, and T6. In both cases, only the stable poles are plotted, and a pole was considered stable when the frequency and damping coefficient estimates from consecutive model orders did not change more than 1% and 5%, respectively, and the MAC was at least 0.99.

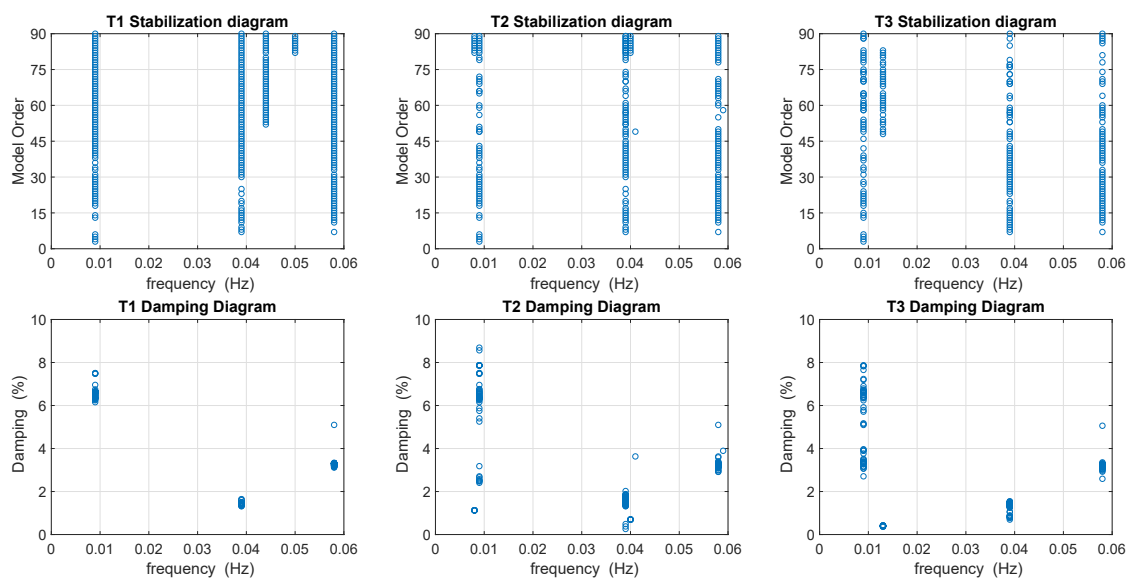


**Figure 3.** Stabilization and damping diagrams for Simulation T1, T2, and T3.

Simulation Scenario T1 is a very simple configuration, where the structure motion can be described by only three degrees of freedom, which is confirmed by the corresponding stabilization and damping diagram, where three independent clusters can be easily identified. In Simulation T2, it is already

possible to identify all the rigid body motions, except for the yaw DOF, still blocked. Although it may not be clear from the stabilization diagram, the presence of the sway and roll modes is easily identified in the damping diagram, where additional clusters can now be seen, associated with lower damping coefficients. The lower value of the damping coefficient of these modes is justified as the waves' incident direction is still perfectly aligned with surge motion, and hence, these motions are associated with poorly excited modes. The same reasoning applies to Simulation T3, where it is now possible to identify the yaw motion frequency for higher model orders at around 0.012 Hz. For all the surge aligned waves, the SSI-COV method is able to correctly identify both the frequency and damping coefficients of all the relevant DOFs.

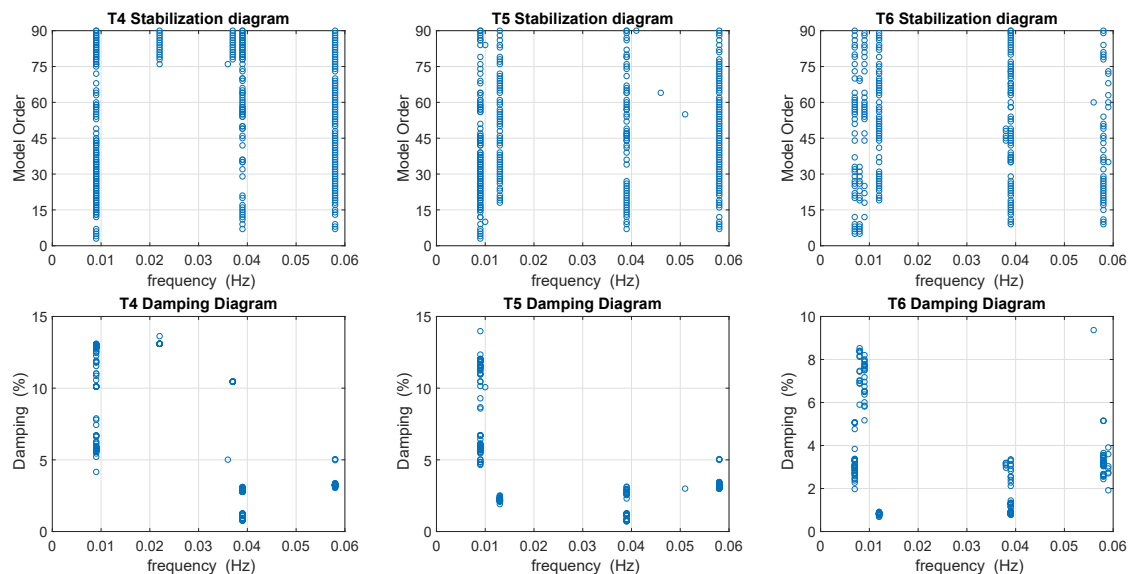


**Figure 4.** Stabilization and damping diagrams for Simulations T4, T5, and T6.

As can be seen in Figure 4, both surge-sway and roll-pitch modes are identified, even in Simulation T4, where their frequency is essentially the same. Once more, the damping diagram reveals the presence of two distinct modes, associated with different damping coefficients. When yaw motions are not restrained (Simulations T5 and T6), an additional peak appears at around 0.012 Hz, consistent with the previously identified yaw frequency in Simulation T3. Because this mode is poorly excited, its corresponding hydrodynamic damping is very low. Finally, when Cable 1's stiffness is modified in Simulation T6, the structure symmetric behavior collapses, and surge and sway frequencies can be identified separately. All the modal properties, including the best estimation for the amplitude of the complex mode shape configurations obtained, are summarized in Table 6, where for Simulations T1, T2, and T3, only the most excited modes have been presented.

From the results presented in Table 6, it can be seen that the frequencies and damping coefficients are consistently obtained from all the simulations. Furthermore, the effect of Cable 1's stiffness modification can be seen in the surge- and sway-dominated modes of Simulation T6. This effect is much more effective for decoupling surge-sway than pitch-roll motions because while the former stiffness is essentially provided by the mooring system, the latter has a strong dependency on hydrodynamic restoring forces, which have not been modified, and so, the platform oscillates around an axis orthogonal to the waves' direction. In order to explore this effect, a new set of simulations was carried out, where the waves' heading direction was gradually changed between  $0^\circ$  and  $90^\circ$ , measured in relation to the surge direction. The relation between surge-sway modal ordinates in the first mode ( $\Phi_{1,1}/\Phi_{2,1}$ ) and roll-pitch modal ordinates in the third mode ( $\Phi_{4,3}/\Phi_{5,3}$ ) is presented in Figure 5.

**Table 6.** Modal properties, including angular frequencies, natural frequencies, modal damping ratios, and 6 mode shape components obtained for the different simulations (X-surge; Y-sway; Z-heave; RX-roll; RY-pitch; RZ-yaw).

Simulation	Mode	$\omega$	$f$	$\zeta$	Mode Shapes Components					
		(mrad/s)	(mHz)	(%)	X	Y	Z	RX	RY	RZ
T1	1	55.3 ± 0.1	8.81 ± 0.02	6.6 ± 0.2	1	0	-0.04	0	0.04	0
	2	245.8 ± 0.1	39.11 ± 0.02	1.47 ± 0.05	0.32	0	0.32	0	1	0
	3	365.6 ± 0.2	58.19 ± 0.04	3.3 ± 0.2	-0.57	0	1	0	-0.08	0
T2	1	55.4 ± 0.2	8.81 ± 0.03	6.5 ± 0.7	1	0	-0.04	0	0.04	0
	2	245.2 ± 0.9	39.0 ± 0.2	1.5 ± 0.4	0.32	0	0.32	0	1	0
	3	365.6 ± 0.9	58.2 ± 0.2	3.3 ± 0.3	-0.56	0	1	0	-0.08	0
T3	1	56.1 ± 0.2	8.92 ± 0.03	6.3 ± 0.8	1	0	-0.03	0	0.04	0
	2	245 ± 1	39.1 ± 0.2	1.3 ± 0.3	0.31	0	0.30	0	1	0
	3	365.4 ± 0.5	58.2 ± 0.1	3.2 ± 0.3	-0.58	0	1	0	-0.07	0
T4	1	55.1 ± 0.3	8.77 ± 0.04	5.9 ± 0.4	0.93	1	-0.04	0.03	-0.04	0
	2	58.0 ± 0.2	9.23 ± 0.04	11.7 ± 1.5	1	0.86	-0.06	-0.03	0.04	0
	3	244 ± 0.4	38.9 ± 0.1	2.9 ± 0.1	-0.46	-0.47	-0.58	1	-0.94	0
	4	246.2 ± 0.3	39.2 ± 0.1	1.0 ± 0.2	-0.21	0.21	0.31	-0.95	1	0
	5	365.5 ± 0.4	58.17 ± 0.06	3.3 ± 0.4	-0.40	-0.40	1	0.03	-0.04	0
T5	1	55.6 ± 0.2	8.84 ± 0.03	5.8 ± 0.5	0.96	1	-0.04	-0.04	0.04	0
	2	58.9 ± 0.3	9.37 ± 0.04	11.2 ± 0.4	1	0.76	-0.07	-0.03	0.04	0.01
	3	79.95 ± 0.09	12.73 ± 0.02	2.2 ± 0.1	0.73	0.77	-0.05	-0.03	0.03	1
	4	244.5 ± 0.6	38.92 ± 0.09	2.8 ± 0.2	-0.51	-0.51	-0.61	1	-0.93	-0.01
	5	246.2 ± 0.3	39.18 ± 0.05	1.0 ± 0.2	-0.20	-0.20	0.30	-0.95	1	-0.01
	6	365.4 ± 0.6	58.15 ± 0.09	3.3 ± 0.4	-0.40	-0.40	1	0.03	-0.04	-0.02
T6	1	46.5 ± 0.2	7.40 ± 0.03	3.3 ± 0.8	1	0.60	-0.02	-0.02	0.03	-0.01
	2	54.2 ± 0.2	8.62 ± 0.03	7.0 ± 0.9	0.78	1	-0.05	-0.03	0.02	-0.02
	3	74.59 ± 0.03	11.87 ± 0.01	0.82 ± 0.05	-0.07	-0.21	-0.04	0.01	-0.01	1
	4	244 ± 2	38.8 ± 0.2	2.9 ± 0.4	0.42	0.42	0.54	-1	1	0
	5	245.7 ± 0.6	39.1 ± 0.1	1.0 ± 0.2	-0.24	-0.20	0.29	-0.93	1	-0.01
	6	366.4 ± 0.9	58.3 ± 0.2	3.3 ± 0.6	-0.47	-0.46	1	0.04	-0.04	-0.02

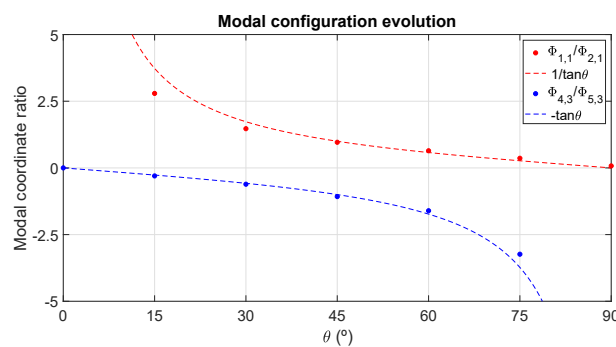


**Figure 5.** Relation between surge and sway modal coordinates for the translation mode (in red) and between the pitch and roll modal coordinates for the rotational mode (in blue).

As can be seen, the response is explained by a translation in the wave’s direction and a rotation around an axis orthogonal to it, as expected considering the indetermination of the mode shapes in the case of an axisymmetric structure. If the same procedure is carried out with the modified cable structure, the translation components’ evolution reveals now significant deviations from the reference scenario, as can be seen in Figure 6, where the red and black dots represent the relation between the surge and sway modal coordinates for the first two modes, respectively, and present higher deviations from the wave incident direction.

Finally, the wave amplitude effect was evaluated. Although a white noise spectrum was used in the presented simulations, the spectrum amplitude depends on the significant wave height. Two additional wave series were generated, where the spectral amplitude was divided and multiplied by four, the results being presented in Figure 7. While the natural frequencies do not appear to change, it seems that the effective damping coefficients are higher for higher significant wave heights, validating the potential of OMA to identify variations of the damping coefficients with the operating conditions of the platform.

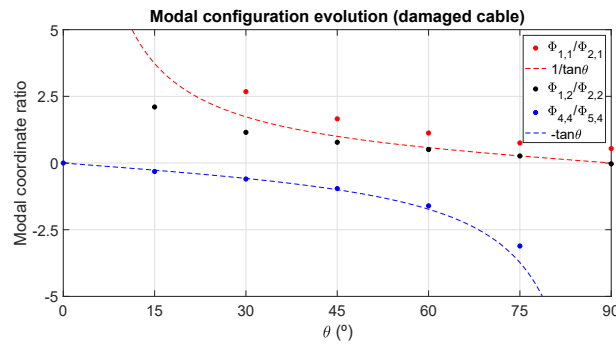


**Figure 6.** Relation between surge and sway modal coordinates for the first (in red) and second (in black) modes and between the pitch and roll modal coordinates for the rotational mode (in blue) considering the damaged cable.

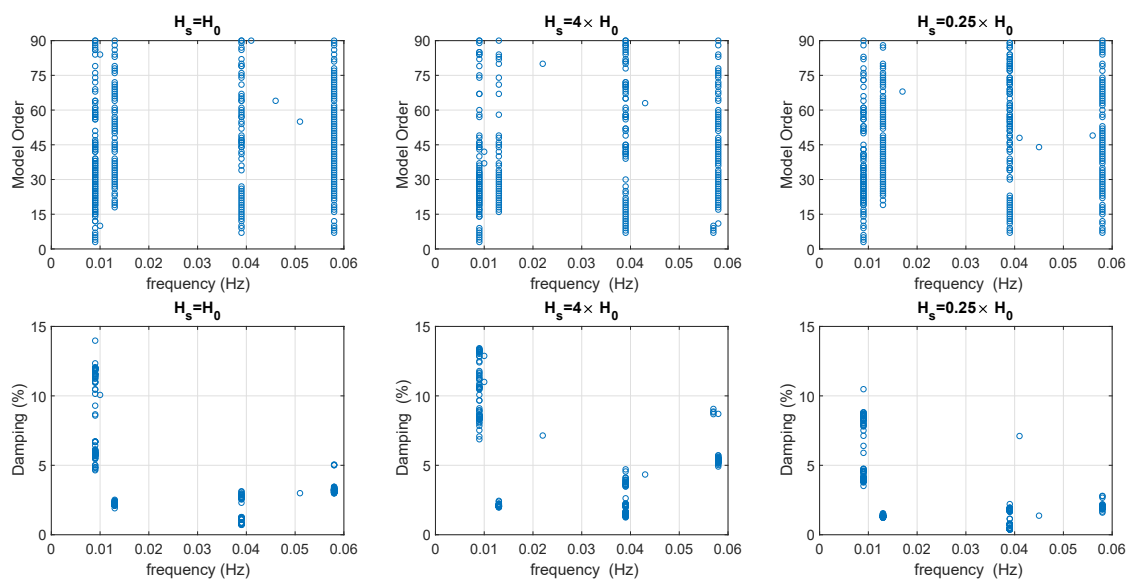


**Figure 7.** Stabilization and damping diagrams for the different wave heights.

#### 4.2. UMaine-Hywind 5 MW Spar Model

From the UMaine-Hywind 5 MW spar numerical model, forty independent time series of 20,000 in length were generated, from which the first 2000 s were once more rejected, leaving a full set of 5 h suitable for analysis. The generated waves followed a JONSWAP spectrum with 10 s peak period and 6 m characteristic height, and the response was sampled at 2.5 Hz.

Before proceeding to the automated analysis of all the generated responses, it is necessary to calibrate the time length to use when computing the autocorrelation function. To do so, a single setup was selected and the stabilization diagram generated for different time intervals, as presented in Figure 8, where a pole was considered stable when the frequency and damping coefficient did not change for a value larger than 1% and 5%, respectively, while the MAC between two model orders was at least 0.99.

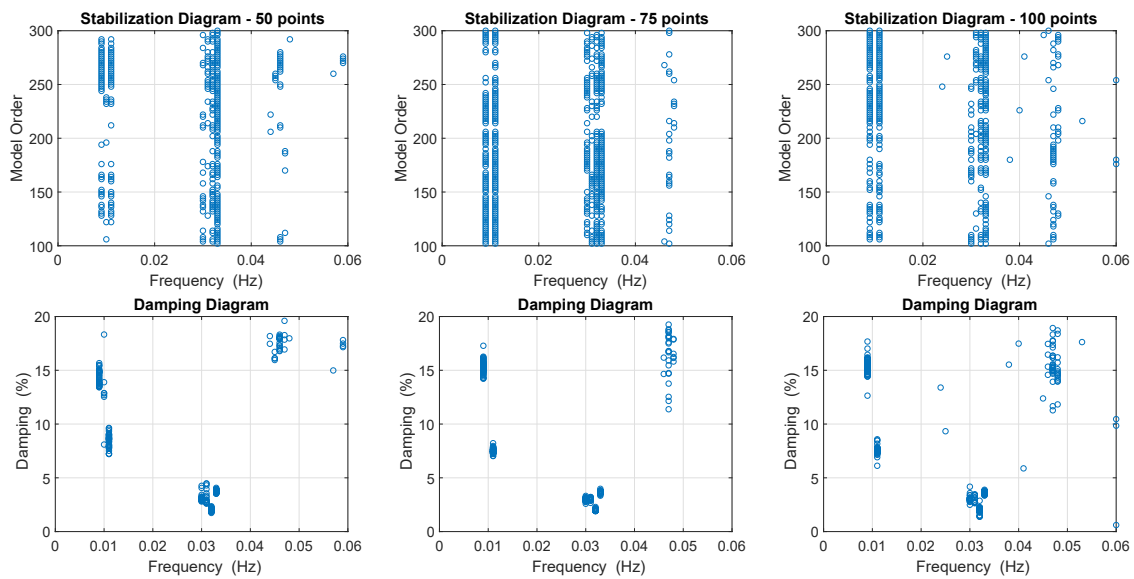


**Figure 8.** Stabilization and damping diagrams obtained considering 50 points (on the left), 75 points (in the middle), or 100 points (on the right) for the autocorrelation function length.

From the plotted stabilization diagrams, it seems that the intermediate value of 75 points provides the best compromise between the quality of higher and lower frequency, and so an autocorrelation function with 75 points will be used in the following analysis.

The analysis of a significant number of setups can be made using a single correlation matrix, obtained by averaging over all the correlation matrices of each setup. The results obtained are plotted in Figure 9 and summarized in Table 7, where the yaw mode has not been included since it is poorly excited and its expected frequency is outside the analyzed frequency range.

**Table 7.** Modal properties, including angular frequencies, natural frequencies, modal damping ratios, and 6 mode shape components obtained with the SSI-COV method, joined analysis of all datasets.

Mode	$\omega$ (mrad/s)	f (mHz)	$\zeta$ (%)	Mode Shapes Components					
				X	Y	Z	RX	RY	RZ
1	$58.85 \pm 0.18$	$9.367 \pm 0.027$	$15.08 \pm 0.58$	1	0.93	0.20	0	0	0.01
2	$68.63 \pm 0.21$	$10.922 \pm 0.032$	$8.61 \pm 0.22$	0.70	1	0.16	0	0	0.01
3	$192.06 \pm 0.09$	$30.567 \pm 0.014$	$2.04 \pm 0.05$	-0.28	0.27	1	-0.02	0.04	0.01
4	$199.32 \pm 0.14$	$31.723 \pm 0.021$	$3.25 \pm 0.08$	-0.12	-0.19	1	-0.02	0.02	0.01
5	$208.99 \pm 0.11$	$33.261 \pm 0.018$	$3.90 \pm 0.07$	0.01	0.03	1	0	0	0.01

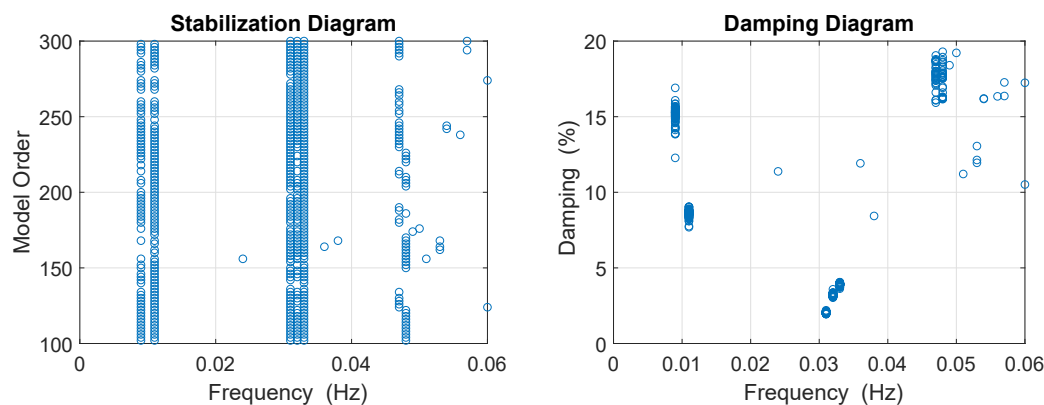


**Figure 9.** Stabilization (on the left) and damping (on the right) diagram obtained from an averaged autocorrelation matrix.

While this procedure allows for the appreciation of a single stabilization, the loss of information is inescapable, as the variations over setups can no longer be seen. However, the automated procedures introduced in Section 2.2 provide the means to overcome this difficulty. As long as the stabilization and cluster definition criteria and reference mode properties are prescribed, the natural frequencies and damping coefficients can be tracked through all the setups. The results obtained for the 40 5h setups are plotted in Figure 10, where different modes are represented in different colors, and it can be seen that the frequencies are consistently obtained throughout the setups while the damping coefficients present higher variability.

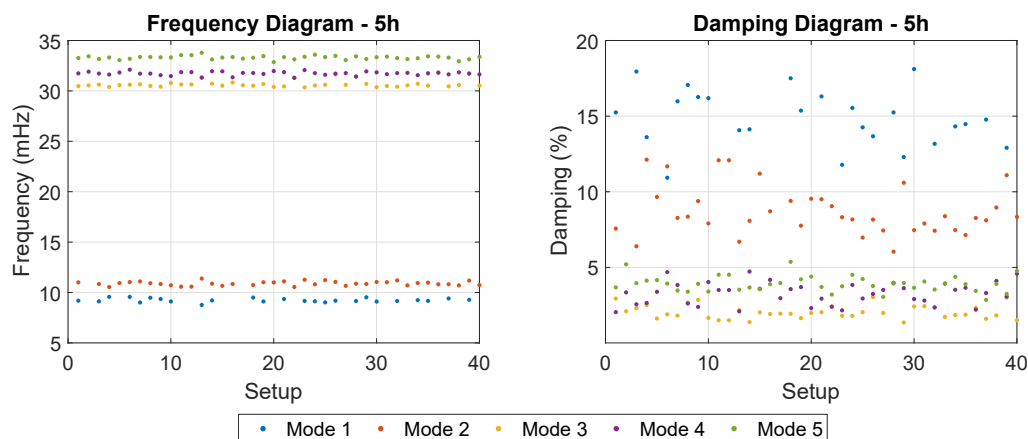


**Figure 10.** Evolution of the mode frequencies (on the left) and damping coefficients (on the right) in the different setups grouped by color.

To further test this methodology and the time series duration's influence on the results, the 200 h of available data were grouped considering 0.5 h, 1 h, 2.5 h, and 5 h setups. The results obtained are summarized in Table 8. While the frequency mean value is consistently obtained, its dispersion is reduced with the increasing length of recorded time. The damping coefficient estimations, both the mean value and dispersion, are more significantly affected. The identified modal damping ratios and frequencies' mean values are correctly identified within all datasets. If this is ensured, the use of a shorter dataset is preferable, since it is easier to ensure stationarity within the dataset.

**Table 8.** Mean values and standard deviation obtained from the automated SSI-COV method.

Mode	0.5 h		1 h		2.5 h		5 h	
	f (mHz)	$\zeta$ (%)						
1	9.2 ± 0.4	11.4 ± 5.1	9.3 ± 0.4	13.3 ± 5.2	9.4 ± 0.4	14.3 ± 4.1	9.4 ± 0.3	15.1 ± 2.1
2	11.0 ± 0.5	7.0 ± 3.7	11.0 ± 0.4	7.9 ± 3.3	10.9 ± 0.3	8.8 ± 3.3	10.9 ± 0.2	8.7 ± 1.6
3	30.8 ± 0.7	2.3 ± 1.7	30.8 ± 0.6	2.3 ± 1.2	30.9 ± 0.5	2.4 ± 0.9	30.7 ± 0.4	2.1 ± 0.5
4	31.8 ± 1.0	2.7 ± 1.6	31.7 ± 0.7	2.7 ± 1.2	31.8 ± 0.5	3.1 ± 0.9	31.7 ± 0.2	3.3 ± 0.7
5	33.6 ± 0.6	4.0 ± 1.7	33.4 ± 0.4	4.0 ± 1.2	33.3 ± 0.2	3.9 ± 0.8	33.3 ± 0.2	3.9 ± 0.5

The results from Table 8 are more easily analyzed and compared with the theoretical values from Table 4 using a boxplot representation. Figure 11 represents the results for the surge, pitch, and heave modal properties. Comparing the identified frequencies and damping coefficients with the theoretical values from Table 4, it is evident that the tools used for automated operational modal analysis are able to track the modal properties throughout.

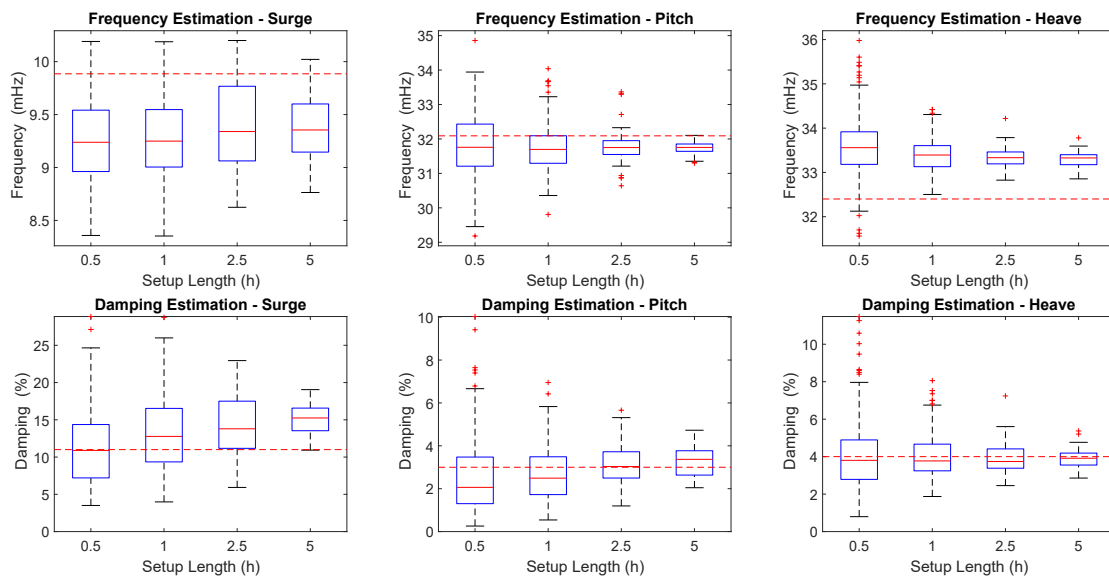


**Figure 11.** Boxplot representation of surge, pitch, and heave modal properties, where the red dots represent outliers' values, and the theoretical values from Table 4 are represented by a red dashed line.

## 5. Conclusions

In this paper, an extensive numerical analysis is described, in order to assess the applicability of the SSI-COV output-only identification technique to identify the modal properties associated with the rigid body motions of floating structures. In particular, two reference 5 MW wind turbines, namely the OC4-DeepCwind semi-submersible platform and UMaine-Hywind spar, were modeled in ANSYS® AQWA, and the time histories of the rigid body motions were obtained, under various simplifying assumptions. Then, the SSI-COV method was applied, to identify the dynamic properties of the models. Based on the interpretation of the results, the following conclusions can be drawn.

- The method proposed is able to identify the modal properties, also in the case of coupled DOFs.
- The method is able to deal with the nonlinearity introduced by the viscous forces in the first case study, as the estimated damping depends on significant wave height.
- If the structure is axisymmetric, the mode shapes are undetermined. This limitation was overcome in the numerical setup by considering a damaged mooring line, i.e., asymmetric stiffness matrix. However, the impact of this shortcoming on real application cases is expected to be reduced, as real structures are not perfectly symmetrical.
- Mode identification changes with wave direction. This variation is consistent with the physics of the platform motion and may be used to detect damaged mooring system conditions.
- The adoption of realistic narrow-banded wave spectra makes the results' interpretation more challenging; however, acceptable results were obtained for sufficiently long motion time histories.
- Automated tracking of modal properties in the context of continuous dynamic monitoring is possible, and adequate results for natural frequencies and modal damping ratios could be obtained with 30 min time series.
- The estimation of damping coefficients is important to identify modes with similar natural frequencies, as the mode shapes were not always clear.

The results obtained pave the way toward direct application of the SSI-COV output-only identification method to the measured time-histories of real floating structure motions, subject to uncontrolled environmental loads. This task will be carried out in the near future by the authors, based on open-sea experiments on floating structures. This would represent an important step for the implementation of intermediate-scale experiments of floating structures at sea, which could significantly ease the development and industrialization of floating structure concepts, as well as serving as a structural health monitoring tool for existing floating structures.

**Author Contributions:** Conceptualization, F.M., C.R., and G.F.; validation, F.M., C.R., G.F., F.A., and M.A.; formal analysis, F.P.; writing, original draft preparation, F.P. and C.R.; writing, review and editing, C.R. and F.M.; funding acquisition, F.M., M.A., and F.A. All authors read and agreed to the published version of the manuscript.

**Funding:** This work was financially supported by: PhD Grant SFRH/BD/138980/2018, Base Funding UIDB/04708/2020 of the CONSTRUCT-Instituto de I&D em Estruturas e Construções and the project PTDC/ECI-EST/29558/2017, funded by national funds through the FCT/MCTES (PIDDAC). The second author's (C.R.) work was conducted with the support of European Commission, European Social Fund and "Regione Calabria", under the project "POR Calabria FESR FSE 2014-2020 Asse Prioritario 12 Azione 10.5.12 Linea B di cui alle Linee Guida "Mobilità internazionale per dottorandi e assegni di ricerca/ricercatori"". The content of the paper and the use of the results here reported are solely the responsibility of the authors and do not necessarily represent the official views of the European Commission and "Regione Calabria".

**Conflicts of Interest:** The authors declare no conflict of interest.

## Abbreviations

The following abbreviations are used in this manuscript:

DOF	Degree Of Freedom
FAST	Fatigue, Aerodynamics, Structures, and Turbulence
FDD	Frequency Domain Decomposition
FOWT	Floating Offshore Wind Turbine
NREL	National Renewable Energy Laboratory
MAC	Modal Assurance Criterion
MPP	Multi-Purpose Platform
OMA	Operational Modal Analysis
SSI-COV	Covariance-driven Stochastic Subspace Identification
SWL	Still Water Level
TRL	Technology Readiness Level
VLFS	Very Large Floating Structures
LCOE	Levelized Cost of Energy

## References

1. Failla, G.; Arena, F. New perspectives in offshore wind energy. *Philos. Trans. R. Soc. A Math. Phys. Eng. Sci.* **2015**, *373*, 20140228. [[CrossRef](#)]
2. Wang, X.; Zeng, X.; Li, J.; Yang, X.; Wang, H. A review on recent advancements of substructures for offshore wind turbines. *Energy Convers. Manag.* **2018**, *158*, 103–119. [[CrossRef](#)]
3. Arrambide, I.; Zubia, I.; Madariaga, A. Critical review of offshore wind turbine energy production and site potential assessment. *Electr. Power Syst. Res.* **2019**, *167*, 39–47. [[CrossRef](#)]
4. Díaz, H.; Guedes Soares, C. Review of the current status, technology and future trends of offshore wind farms. *Ocean Eng.* **2020**, *209*, 107381. [[CrossRef](#)]
5. Brincker, R.; Zhang, L.; Andersen, P. Modal identification from ambient responses using frequency domain decomposition. In Proceedings of the 18th International Modal Analysis Conference (IMAC), San Antonio, TX, USA, 7–10 February 2000.
6. Roddier, D.; Cermelli, C.; Aubault, A.; Weinstein, A. WindFloat: A floating foundation for offshore wind turbines. *J. Renew. Sustain. Energy* **2010**, *2*, 033104. [[CrossRef](#)]
7. Flikkema, M.; Waals, O. Space@Sea the Floating Solution. *Front. Mar. Sci.* **2019**, *6*, 553. [[CrossRef](#)]
8. Lagasco, F.; Collu, M.; Mariotti, A.; Safier, E.; Arena, F.; Atack, T.; Brizzi, G.; Tett, P.; Santoro, A.; Bourdier, S.; et al. New Engineering Approach for the Development and Demonstration of a Multi-Purpose Platform for the Blue Growth Economy. In Proceedings of the ASME 2019 38th International Conference on Ocean, Offshore and Arctic Engineering, Glasgow, UK, 9–14 June 2019. [[CrossRef](#)]
9. Wang, C.; Tay, Z. Very Large Floating Structures: Applications, Research and Development. *Procedia Eng.* **2011**, *14*, 62–72. [[CrossRef](#)]
10. Lamas-Pardo, M.; Iglesias, G.; Carral, L. A review of Very Large Floating Structures (VLFS) for coastal and offshore uses. *Ocean Eng.* **2015**, *109*, 677–690. [[CrossRef](#)]

11. Li, L.; Collu, M.; Ruzzo, C.; Failla, G.; Abhinav, K.A.; Arena, F. Analysis of the Coupled Dynamics of an Offshore Floating Multi-Purpose Platform: Part A—Rigid Body Analysis. In Proceedings of the ASME 2019 38th International Conference on Ocean, Offshore and Arctic Engineering, Glasgow, UK, 9–14 June 2019. [[CrossRef](#)]
12. Ruzzo, C.; Failla, G.; Arena, F.; Collu, M.; Li, L.; Mariotti, A. Analysis of the Coupled Dynamics of an Offshore Floating Multi-Purpose Platform: Part B—Hydro-Elastic Analysis with Flexible Support Platform. In Proceedings of the ASME 2019 38th International Conference on Ocean, Offshore and Arctic Engineering, Glasgow, UK, 9–14 June 2019. [[CrossRef](#)]
13. Stuyfzand, P.J.; Kappelhof, J.W. Floating, high-capacity desalting islands on renewable multi-energy supply. *Desalination* **2005**, *177*, 259–266. [[CrossRef](#)]
14. Itiki, R.; Di Santo, S.G.; Itiki, C.; Manjrekar, M.; Chowdhury, B.H. A comprehensive review and proposed architecture for offshore power system. *Int. J. Electr. Power Energy Syst.* **2019**, *111*, 79–92. [[CrossRef](#)]
15. Goupee, A.; Koo, B.; Lambrakos, K.; Kimball, R. Model Tests for Three Floating Wind Turbine Concepts. *Offshore Technol. Conf. Proc.* **2012**, *3*. [[CrossRef](#)]
16. Shin, H.; Dam, P.T.; Jung, K.J.; Song, J.; Rim, C.; Chung, T. Model test of new floating offshore wind turbine platforms. *Int. J. Nav. Archit. Ocean Eng.* **2013**, *5*, 199–209. [[CrossRef](#)]
17. Duan, F.; Hu, Z.; Niedzwecki, J. Model test investigation of a spar floating wind turbine. *Mar. Struct.* **2016**, *49*, 76–96. [[CrossRef](#)]
18. Ruzzo, C.; Muggiasca, S.; Malara, G.; Taruffi, F.; Belloli, M.; Collu, M.; Brizzi, L.L.G.; Arena, F. Scaling strategies for multi-purpose floating structures physical modeling: State of art and new perspectives. *Appl. Ocean Res.* **2020**. Under review.
19. Ruzzo, C.; Fiamma, V.; Collu, M.; Failla, G.; Nava, V.; Arena, F. On intermediate-scale open-sea experiments on floating offshore structures: Feasibility and application on a spar support for offshore wind turbines. *Mar. Struct.* **2018**, *61*. [[CrossRef](#)]
20. Ruzzo, C.; Saha, N.; Arena, F. Wave spectral analysis for design of a spar floating wind turbine in Mediterranean Sea. *Ocean Eng.* **2019**, *184*, 255–272. [[CrossRef](#)]
21. Robertson, A.; Jonkman, J. Loads Analysis of Several Offshore Floating Wind Turbine Concepts. In Proceedings of the International Offshore and Polar Engineering Conference, Maui, HI, USA, 19–24 June 2011.
22. Magalhães, F.; Álvaro, C. Explaining operational modal analysis with data from an arch bridge. *Mech. Syst. Signal Process.* **2011**, *25*, 1431–1450. [[CrossRef](#)]
23. Ruzzo, C.; Failla, G.; Collu, M.; Nava, V.; Fiamma, V.; Arena, F. Operational Modal Analysis of a Spar-Type Floating Platform Using Frequency Domain Decomposition Method. *Energies* **2016**, *9*, 870. [[CrossRef](#)]
24. Ruzzo, C.; Failla, G.; Collu, M.; Nava, V.; Fiamma, V.; Arena, F. Output-only identification of rigid body motions of floating structures: A case study. *Procedia Eng.* **2017**, *199*, 930–935. [[CrossRef](#)]
25. Robertson, A.; Jonkman, J.; Masciola, M.; Song, H.; Goupee, A.; Coulling, A.; Luan, C. *Definition of the Semisubmersible Floating System for Phase II of OC4*; Technical Report; National Renewable Energy Lab. (NREL): Golden, CO, USA, 2014.
26. Peeters, B.; De Roeck, G. Reference-based stochastic subspace identification for output-only modal analysis. *Mech. Syst. Signal Process.* **1999**, *13*, 855–878. [[CrossRef](#)]
27. Overschee, P.V.; Moor, B.D. *Subspace Identification for Linear Systems*; Kluwer Academic Publishers: Leuven, Belgium, 1996.
28. Magalhães, F.; Cunha, A.; Caetano, E. Online automatic identification of the modal parameters of a long span arch bridge. *Mech. Syst. Signal Process.* **2009**, *23*, 316–329. [[CrossRef](#)]
29. Pastor, M.; Binda, M.; Harčarik, T. Modal assurance criterion. *Procedia Eng.* **2012**, *48*, 543–548. [[CrossRef](#)]
30. Jonkman, J.; Butterfield, S.; Musial, W.; Scott, G. *Definition of a 5-MW Reference Wind Turbine for Offshore System Development*; Technical Report; National Renewable Energy Lab. (NREL): Golden, CO, USA, 2009.
31. Ruzzo, C. A New Approach for Intermediate-Scale Open-Sea Experimental Activities on Offshore Structures: Application to Spar Buoys for Wind Energy Exploitation via a 1:30 Scale Activity. Ph.D. Thesis, Mediterranean University of Reggio Calabria, Reggio Calabria, Italy, 2016.

32. Jonkman, J. *Definition of the Floating System for Phase IV of OC3*; Technical Report; National Renewable Energy Lab. (NREL): Golden, CO, USA, 2010.
33. Siow, C.; Koto, J.; Abyn, H.; Khairuddin, N. Linearized Morison Drag for Improvement Semi-Submersible Heave Response Prediction by Diffraction Potential. *J. Ocean. Mech. Aerosp. Sci. Eng.* **2014**, *6*, 8–16.

**Publisher's Note:** MDPI stays neutral with regard to jurisdictional claims in published maps and institutional affiliations.



© 2020 by the authors. Licensee MDPI, Basel, Switzerland. This article is an open access article distributed under the terms and conditions of the Creative Commons Attribution (CC BY) license (<http://creativecommons.org/licenses/by/4.0/>).